

X-ray induced grain structure dynamics in Bi₂Se₃

Kento Katagiri^{1,2,3*}, Bernard Koziolowski⁴, Eric Folsom⁴, Yifan Wang^{1,2,3}, Karen Appel⁵,
Philip K. Cook⁶, Jon Eggert⁴, Sebastian Göde⁵, Marylesa Howard⁷, Sungwon Kim⁸,
Mikako Matsuda⁵, Motoaki Nakatsutsumi⁵, Martin M. Nielsen⁹, Henning F. Poulsen⁹,
Frank Seiboth¹⁰, Hugh Simons⁹, Bihan Wang¹¹, Wenge Yang¹¹, Ulf Zastrau⁵, Hyunjung Kim⁸,
and Leora E. Dresselhaus-Marais^{1,2,3,4*}

¹*Stanford University, Department of Materials Science and Engineering, California 94305, USA*

²*SLAC National Accelerator Laboratory, California 94025, USA*

³*Stanford University, PULSE Institute, Stanford, California 94305, USA*

⁴*Lawrence Livermore National Laboratory, California 94550, USA*

⁵*European XFEL GmbH, Schenefeld 22869, Germany*

⁶*University of Natural Resources and Life Sciences (BOKU), Institute for Physics and Materials Science, Vienna 1190, Austria*

⁷*Nevada National Security Site, Nevada 89030, USA*

⁸*Sogang University, Department of Physics, Seoul 04107, Korea*

⁹*Technical University of Denmark, Department of Physics, Kgs. Lyngby 2800, Denmark*

¹⁰*Center for X-ray and Nano Science CXNS, Deutsches Elektronen-Synchrotron DESY, Notkestr. 85, Hamburg 22607, Germany*

¹¹*Center for High-Pressure Science and Technology Advanced Research, Shanghai 201203, China*

*Corresponding authors. Email: kentok@stanford.edu & leoradm@stanford.edu

Grain rotation in crystals often results in coarsening or refinement of the grains that modify the mechanical and thermal properties of materials. While many studies have explored how externally applied stress and temperature drive grain structure dynamics in nanopolycrystalline materials, the analogous studies on colossal grains have been limited, especially in the absence of external force. In this work, we used X-ray free electron laser pulses to irradiate single-crystalline bismuth selenide (Bi_2Se_3) and observed grain boundary formation and subsequent grain rotation in response to the X-ray radiation. Our observations with simultaneous X-ray diffraction and transmission X-ray microscopy demonstrate how intense X-ray radiation can rapidly change grain morphologies of initially single-crystalline material.

1. Introduction

Understandings of grain motion dynamics and resulting changes in their morphologies are essential to accurately model deformation processes [1-4] and to control the mechanical properties of materials [5,6]. Previous *in-situ* experiments have observed grain motions mostly with transmission electron microscope (TEM) or X-ray diffraction (XRD) measurements. TEM can provide the nanometer-scale spatial resolution required to resolve the detailed structure of the lattices and dislocation behaviors in grains and near grain boundaries [7-13]. Recent advances in the TEM techniques have also enabled dynamic observation with a high temporal resolution down to hundreds of femtoseconds [14]. However, because of the strict requirements for sample thickness and the enclosed vacuum environments, some *in-situ* experiments are difficult to perform. As such, X-ray experiments at synchrotron and X-ray free electron laser (XFEL) sources are frequently performed to understand the dynamics of grain boundaries and grain rotation during mechanical testing. XRD measurements using those high-intensity and short-pulsed X-ray sources typically probe the samples for high reciprocal space [15-17] and temporal resolution [18], down to sub-micrometers and picoseconds, respectively. Nevertheless, XRD spatially integrates the lattice information to resolve its reciprocal space details over the illuminated volume, resulting in low real-space resolution, or a requirement for long-duration mapping scan [19,20]. For these reasons, XRD and TEM observations have been complementary to each other for experimental studies on grain structure dynamics.

Previous works including experiments, theory, and simulations have revealed the following characteristics of grain structure dynamics in materials: (1) The grain rotation rate increases as the grain size decreases, with a dependence of d^{-n} where d is the grain size and n is an index varied between 2 and 5 [5]. (2) The lattice misorientation of adjacent grains at a grain boundary tends to

decrease by grain rotations [21]. (3) The rotation from high-angle grain boundary to low-angle grain boundary (misorientation angle of above and below 15° , respectively) often results in an increase in grain size (termed grain coarsening) [22,23], as it lowers the surface energy of the material [11,24]. These grain-rotation dynamics studies have mainly focused on grain rotations and coarsening of nano-polycrystalline materials that are enabled by the relevant detailed characterization methods. Many of these studies explore grain rotation dynamics of nano-polycrystals to understand effects that could cause the strengthening effects of nanocrystalline materials observed in the Hall-Petch effect to break down. Nonetheless, many applications also need to understand how crystallinity changes at the larger length scale, and thus experimental studies on the grain refinement and grain rotation of initially single-crystalline or micro-polycrystalline forms of materials are expected.

While most of the previous experiments on grain structure dynamics have used externally applied force and temperature to drive the grain motions [15,25,26], recent work has shown that intense radiation of X-rays or ion beams can also activate such grain motions in some polycrystalline materials [27-29]. Radiation-induced modifications of the grain structure are ubiquitous in industrial applications such as spacecraft materials and nuclear reactor walls [30] but its detailed mechanism and effect on the mechanical properties of the material have been elusive. Understanding the dynamics of radiation-induced grain refinement and rotation in a crystal with initially large grains would also lead to the development of a method to enhance the mechanical properties of materials through the Hall-Petch effect.

In this study, we used the high-intensity X-ray pulses generated at European XFEL to irradiate a bismuth selenide (Bi_2Se_3) single crystal and resolved the X-ray induced grain boundary formations and subsequent grain rotations. Using simultaneous transmission X-ray microscopy (TXM) and X-ray diffraction (XRD), we demonstrate how the heat associated with extreme X-ray absorption give rise to grain boundary formation and subsequent grain rotations that increase the surface energy of the material. Our study provides insights into the dynamics of grain structure at micrometer scales and illustrates the up-hill energy processes that can be activated by sufficiently bright X-ray beams.

2. Results and Discussion

The experiment was performed at the High Energy Density (HED) instrument of the European XFEL [31,32]. As shown in Figure 1a, we used the XFEL beam to simultaneously measure XRD and TXM. Though both XRD and TXM measurements can be done non-destructively, the X-ray intensity used in this work was tuned to be high enough to cause damage to the sample. We thus

used the X-ray pulses both as a pump of the sample to activate damage and a probe of the deformations caused by the previous pulses. Using the femtosecond X-ray pulses generated by the XFEL, XRD can resolve the dynamics of structural changes such as lattice deformation, structural transformations, or changes to the crystalline orientation. TXM records the real-space intensity map of the X-ray beam transmitted through the sample, obtaining the highest resolution images among transmission X-ray imaging techniques as has been demonstrated in [34]. For TXM, the X-ray beam transmitted the sample is magnified by using X-ray lenses, in our case compound refractive lenses (CRLs) [35], to form a real-space image in the far-field with a high spatial resolution.

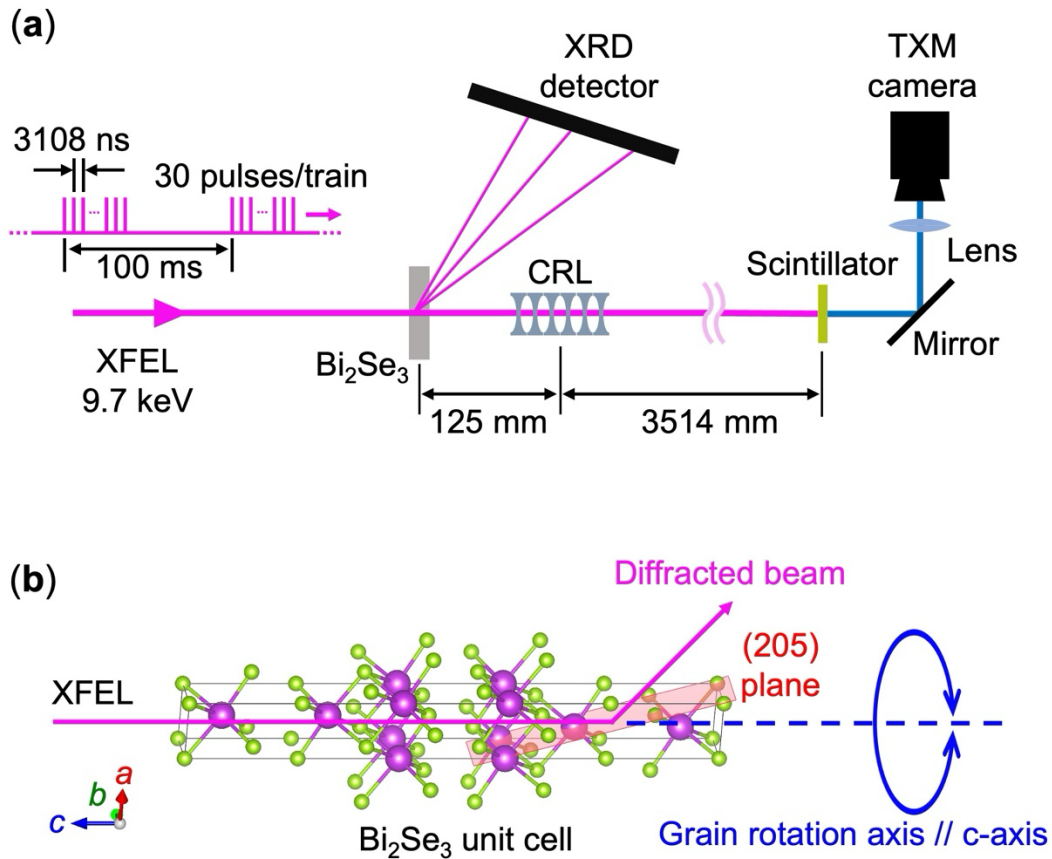


Figure 1. (a) Schematic of the simultaneous X-ray diffraction (XRD) and transmission X-ray microscope (TXM) measurements at the HED instrument of European XFEL. Figures not drawn to scale. (b) The Bi_2Se_3 crystal structure [33] with the XFEL irradiation and diffraction directions. The c -axis of Bi_2Se_3 (normal to the basal plane) is aligned nearly parallel to the X-ray irradiation direction, and the c -axis is also collinear to the grain rotation axis. The purple and light green spheres represent Bi and Se atoms, respectively. The (205) diffraction plane of Bi_2Se_3 is shown as a red plane within the unit cell.

The X-ray pulses we used in this study had a photon energy of $E = 9.7$ keV. The measured XFEL beam size on the Bi_2Se_3 sample was $\sim 32\text{-}\mu\text{m}$ and $\sim 52\text{-}\mu\text{m}$ size in horizontal and vertical directions, respectively. The small beam size was achieved by using 4-jaw slits located $\sim 10\text{-m}$ upstream from the sample. The collimated X-ray beam was separated in time as pulse trains. Each train contained 30 individual X-ray pulses that were evenly spaced in time, and the time interval between each train was 100 ms. The timing interval between each pulse was 3108 ns and the duration of each pulse was ~ 30 fs.

For the XRD setup, the X-ray beams diffracted by the sample were collected by using a 2-dimensional XRD detector (Jungfrau, Paul Scherrer Institut) placed 193 mm downstream of the sample. We placed a $300\text{-}\mu\text{m}$ thick aluminum foil in front of the XRD detector to attenuate some of the XRD signals to avoid saturation of the detector. For the TXM, we placed 50 of 2-D beryllium CRLs ($R = 50\text{-}\mu\text{m}$) along the transmitted beam to magnify the image. $300\text{-}\mu\text{m}$ and $400\text{-}\mu\text{m}$ pinholes were placed at the entrance and exit surfaces of the CRLs, respectively. The magnified image was then converted to visible light by a $35\text{-}\mu\text{m}$ thick LuAG: Ce scintillator, then further magnified with a $7.5\times$ magnification objective lens (Mitutoyo) before it was recorded by a camera (Photonic Science sCMOS 4.2). Our spatial calibration using a 2000-mesh TEM grid indicates the total magnification achieved is $239\times$. While each TXM frame recorded the integration of all 30 pulses from a train, we set the XRD to integrate the diffraction patterns from the last 15 of the 30 pulses for each pulse-train, to efficiently collect diffraction from the heated volume where dislocation motions are more active. Since each train was separated by 100 ms, images were recorded at a frame rate of 10 frames per second for both the XRD and TXM.

A single crystal of Bi_2Se_3 with an initial thickness of $35\text{ }\mu\text{m}$ was placed with normal incidence to the X-ray beam. Our pre-characterization showed the initial structure of our Bi_2Se_3 crystal is $R\text{-}3m$, which is the known stable form of Bi_2Se_3 at ambient conditions [36], and the basal plane of the Bi_2Se_3 was parallel to the sample surface. We used the diffraction peak from the (205) planes of the $R\text{-}3m$ structure of Bi_2Se_3 to track the grain orientation, separation, and rotation. The (205) peak position observed in the XFEL experiment is at $2\theta = 43.8^\circ$ and the theoretical angle between the prismatic and (205) planes of Bi_2Se_3 is $\omega = 19.9^\circ$. This means that a slight modification of the sample placement angle: $2\theta/2 - \omega = 2.0^\circ$ is required to give the diffraction signals (*i.e.*, to satisfy the Bragg condition). This was thought to have occurred by the X-ray induced heating as a strong and spotty XRD peak from the Bi_2Se_3 (205) planes suddenly appeared during the X-ray irradiations (See Movie. S2 [37]). This slight angular offset of the initial orientational was used to avoid saturating the XRD detector with diffraction from the high-

intensity single-crystalline peak of the initial pristine crystal. The quasi-2D layered atomic structure of Bi_2Se_3 crystal makes it easy to control the main grain rotation axis which was predicted, and later confirmed by the experiments, to be normal to its basal plane [38]. By making the grain rotation axis almost collinear to the XFEL irradiation direction (Figure 1b), we were able to track grain rotation as the change in the azimuthal angle of the diffracted peak. If the rotation was not along the X-ray irradiation direction, the XRD peak would disappear when the grain rotates largely in different directions as the rotated grain would no longer satisfy the Bragg condition.

Based on the X-ray pulse energy measured upstream of the beamline, we estimate the pulse energy at the sample to be $\sim 2.5 \mu\text{J}/\text{pulse}$ [37]. Based on this energy, we simulated the spatial distribution of temperature in the Bi_2Se_3 crystal induced by irradiation from one X-ray pulse train (30 pulses), as shown in Figure 2a. Our simulation results suggest the temperature rise after irradiation of one X-ray pulse train would reach $\sim 1600 \text{ K}$ near the irradiated surface of the sample. As the melting temperature of Bi_2Se_3 is 978 K [39], we predict the X-ray irradiation caused the irradiated volume of the crystal to partially melt. The simulated temperature in Bi_2Se_3 also reaches the vaporization temperature which is estimated to be around 1600 K based on extrapolation of the pressure-dependent vaporization temperature data of [40], but the X-rays do not deliver enough energy to completely vaporize the crystal when considering the latent heat needed for the full vaporization. It is worth noting that Bi_2Se_3 is known to have no high-temperature phase transitions up to its melting temperature at ambient pressure [39]. Our simulation also suggests that the thermal diffusion carries the heat out of the hot spot in less than 100 ms (Figure 2b). This indicates that the 3108 ns time separation over the full 30 X-ray pulses in each train is short enough to accumulate some heat in the crystal, while the 100 ms interval between each train is long enough to fully cool down the heat.

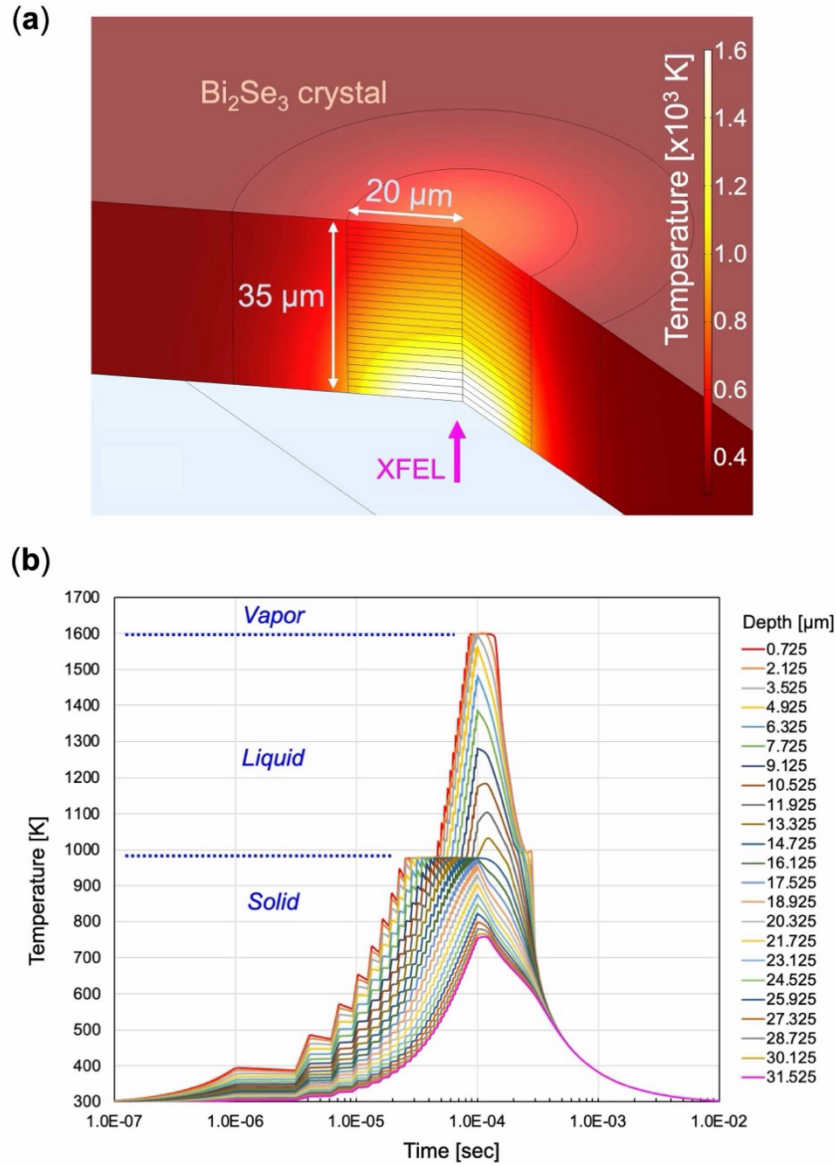


Figure 2. Temperature simulations based on the estimated on-sample XFEL pulse energy. This simulation considers one pulse train that contains 30 XFEL pulses with a time spacing of 3108 ns between each pulse. **(a)** Simulated spatial temperature distribution at the end of the irradiation of one pulse train. **(b)** Time dependence of the simulated temperatures at different depths from the XFEL irradiated side of the crystal surface.

Some TXM images are displayed in Fig. 3 to show the time-dependence of the X-ray-induced damage on the Bi_2Se_3 crystal. See Movie. S1 [37] for the complete set of the recorded TXM images (0-20 s, 10 fps). At 14.9 s and after, a large hole is observed in the center of the irradiated volume, indicating the X-ray induced damage fully penetrates through the depth of the crystal. Before the penetration completes, some of the TXM images capture the formation of small

circular features, as indicated by the red arrows in Figure 3. The sizes of the features are up to several micrometers in diameter and once they appear, each feature remains for 1-3 image frames (0.1-0.3 s) at the same position without changing their sizes before disappearing. We interpret these circular features to be bubbles resulting from the vaporized Bi_2Se_3 formed at the surface or trapped in the sub-surface of the crystal. Although our simulation (Fig. 2) indicates the maximum temperature in the crystal to be slightly lower than the vaporization temperature, the non-uniformity of the spatial intensity distribution of the X-ray pulse should give rise to non-uniformity of the temperature distribution, which would likely give rise to vaporization at local hotspots. We note that these bubble features tend to emerge in the brightest regions of our X-ray images, which is consistent with this interpretation. We also note that some of the TXM images we collected showed weaker signals compared to the others, indicating that there is some pulse-by-pulse fluctuation of the on-target XFEL pulse energy which also could contribute to the local vaporization of the crystal.

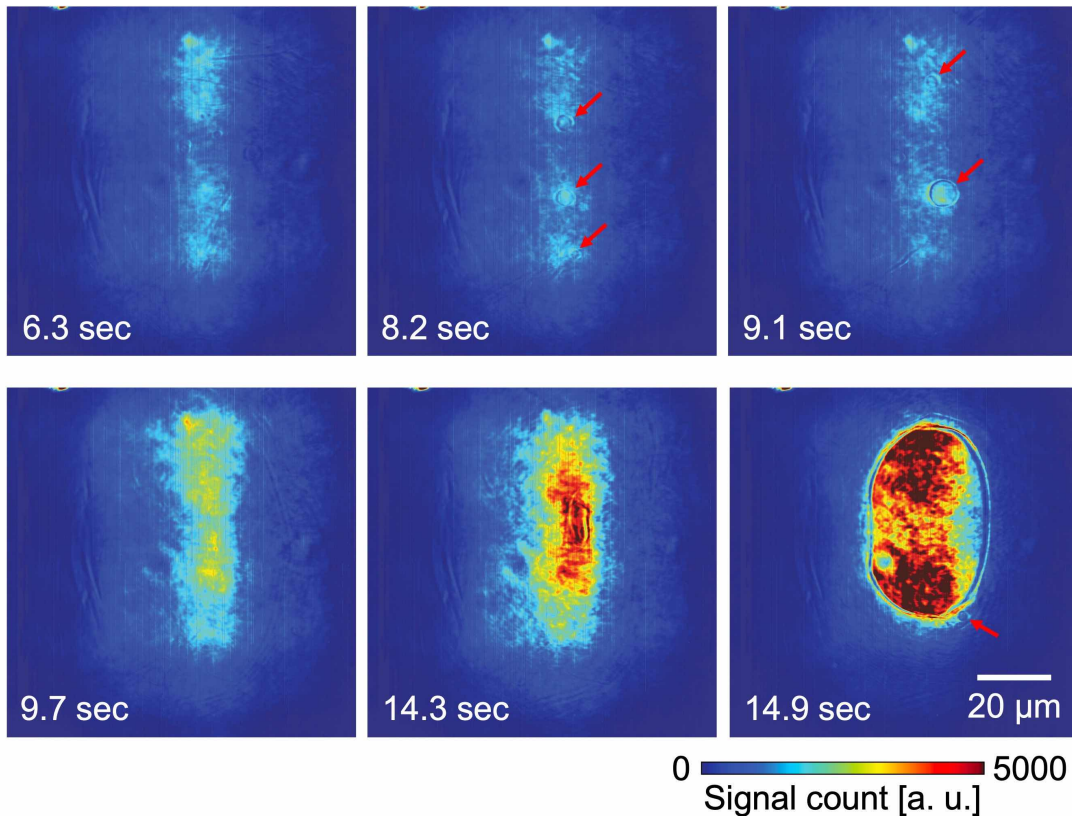


Figure 3. TXM images showing time-dependence of the X-ray-induced damage on the Bi_2Se_3 crystal. The 0 s denotes the timing of the first X-ray train irradiation on the crystal. The observed signal counts increase as the time progresses, as the X-ray irradiated volume of the crystal becomes thinner by the X-ray induced damage. A large penetration hole is observed at 14.9 s.

The red arrows indicate the appearance of the transient formation of bubbles. The scale bar on the 14.9 s image shows the scale at the imaging plane (*i.e.*, the scale at the sample, not at the detector).

Some of the recorded XRD images showing the time evolution of the grain boundary formations and subsequent grain rotations in the Bi_2Se_3 crystal are shown in Figure 4. See Movie S2 [37] also for the complete set of the recorded XRD images (0-20 s, 10 fps). The XRD images show how a spotty diffraction peak from the (205) plane observed at a scattering angle of $2\theta \cong 44^\circ$ splits into three spots and then changes their azimuthal positions by the subsequent XFEL irradiation. The strong (205) diffraction peak observed at 8.1 s separates into three different peaks at 8.3 s, indicating one large grain splitting into three or more smaller grains by forming subgrain boundaries (also known as low-angle grain boundaries). Then the subsequent changes of the observed peak positions in azimuthal angle observed at 8.4 s and after show the grains rotating towards the formations of high-angle grain boundaries.

A closer look at the XRD peaks (Figure 4) shows the broadening of the diffraction rings in 2θ directions which is especially evident for the strongest diffraction peaks from the (205) planes. This should be the result of lattice expansion [41] caused by temperature increases. As we set each XRD image acquisition to accumulate the diffraction patterns from the last 15 XFEL pulses of the 30 pulses in each train, each XRD image records the sum of the diffraction signals from the same crystal but at 15 different states with a slight temperature increase between each pulse. Since the temperature increment causes the crystal to expand, the latest pulses should diffract to smaller 2θ values than the earlier pulses, resulting in the observed broadening of the diffraction peaks in the 2θ direction.

While our temperature simulation suggests some fraction of the Bi_2Se_3 crystal to be melted under the X-ray induced heat, our XRD detected no sign of liquid scattering. This is thought to be because the volume fraction of the melted portion relative to the part remaining solid is small.

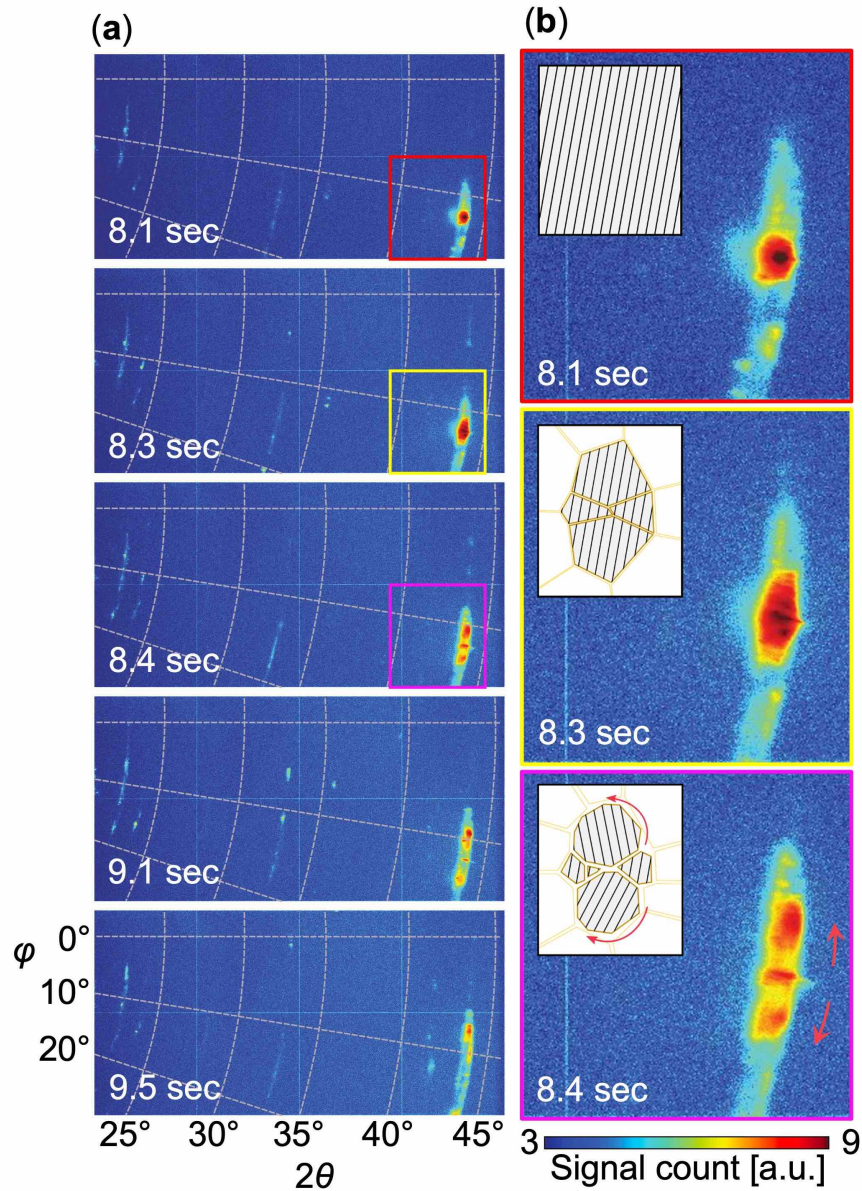


Figure 4. Grain boundary formation and subsequent grain rotation of Bi_2Se_3 time-resolved by the XRD. All images shown in this figure are log-scaled. The noted times correspond to those for the TXM images in Figure 3. **(a)** XRD images taken at five representative times. **(b)** Some of the images of (a) enlarged to show the detail of the XRD peak from (205) planes. Red arrows indicate the direction of the rotation along the azimuthal direction. Insets are cartoons describing a possible explanation of the grain boundary formation and subsequent grain rotation sequences observed by the XRD.

As the measured XRD is time-resolving the rotation of the grains with 10 fps, the speed of the grain rotation can be determined. Figure 5a shows the azimuthal position of the (205) diffraction peak as a function of time and Figure 5b shows the measured traces of the peak positions. By taking the derivative of the change of the azimuthal angles of the traces, we obtained the angular velocities of the Bi_2Se_3 grain rotations (Figure 5c). The fastest grain rotation speed observed in this work is 8.6 deg/s. Huang *et al.* reported the grain rotation speed in nano-polycrystalline AgBr induced by irradiation of synchrotron X-rays reached 186 deg/s [27]. They also observed much slower grain rotation of AgBr with a speed comparable to our Bi_2Se_3 results (1-10 deg/s). The faster grain rotation speed observed by Huang *et al.* can be explained by the effect of the smaller grain size of their crystal. Compared to these radiation induced studies, most previous TEM studies that used mechanical stress to induce grain rotations observed slower grain rotations (<0.1 deg/s) for nanograins [8].

The grain fragmentation of nano-polycrystalline AgBr observed by Huang *et al.* [27] was induced by synchrotron X-ray beams focused to nanometers. They found the grain fragmentation was induced by the photo-induced chemical decomposition of AgBr to Ag + Br. They described that the grain fragmentations drive the subsequent grain rotations. In our Bi_2Se_3 study, however, the XRD measurements did not show any sign of the decomposition from Bi_2Se_3 to Bi + Se, as it only recorded the $R\text{-}3m$ structure of the Bi_2Se_3 crystal which is the most stable structure of the Bi_2Se_3 crystal at ambient conditions (Figure S1). Thus, we interpret the driver of the observed grain refining of Bi_2Se_3 to be not the photo-induced chemical decomposition, but the X-ray induced thermal stress built up in the lattice exceeding the yielding stress of Bi_2Se_3 .

We interpret that the grain boundary formation of the Bi_2Se_3 crystal is caused by the X-ray induced thermal stress built up exceeding the elastic limit of the material. The subsequent grain rotation can be explained by the conventional understanding of dislocation-mediated grain rotations [42,43]. It should be noted that our temperature simulations suggest that there is a non-negligible amount of heat diffusion which heats the crystal outside of the X-ray irradiated volume. Our XRD captured some of the diffraction signals from the Bi_2Se_3 sample even after the X-ray beam penetrated the sample. This implies that some grain dynamics are occurring outside of the main beam, contributing to the XRD signals both before and after the penetration. Our TXM also suggests there are some X-ray intensities outside of the main beam, which would contribute to the XRD signals even though those X-rays may not be strong enough to drive the grain structure dynamics. While the XRD signal contributions from inside and outside of the main beam cannot be separated in our schematic as the XRD integrates them, we interpret the dynamics of large grains observed at early stages of irradiation would only occur at the volume irradiated by the

main beam (*i.e.*, inside the volume penetrated at 14.9 s).

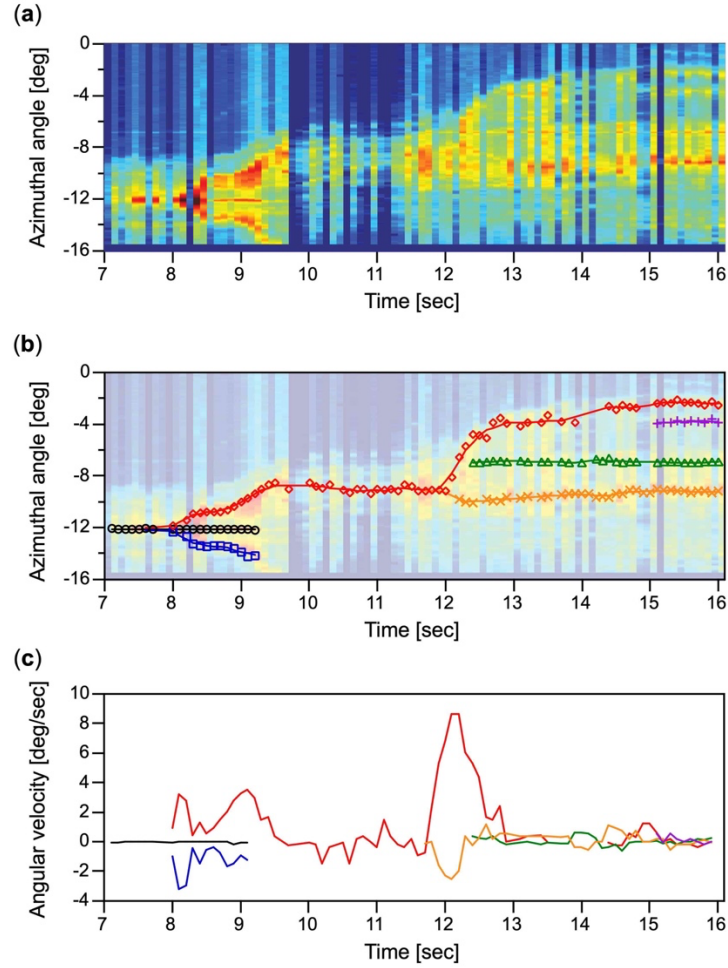


Figure 5. Grain rotation of Bi_2Se_3 observed by the XRD. **(a)** The azimuthal intensity distribution of the diffraction peak from (205) planes. **(b)** Traces of the XRD peak positions observed in (a). Plots are the measured peak positions with different colors and shapes used for different traces. Solid lines are the moving average ($k = 5$) of the measured plots. **(c)** Angular velocities of each trace obtained by taking the derivative of the moving average traces shown in (b). The colors of the lines correspond to those in (b).

3. Conclusions

Grain structure dynamics strongly depend on the size of the grains and thus driving rotations of large (μm or larger) grains requires strong driving forces. Our results experimentally demonstrated that intense X-ray irradiation can induce grain boundary formations and subsequent grain rotations in single crystalline Bi_2Se_3 . Our results offer new insights into the design of

shielding materials experiencing significant radiation-induced damages, as well as into the X-ray irradiation-driven grain refinement process for enhancing the mechanical properties of materials.

Acknowledgements

We acknowledge European XFEL in Schenefeld, Germany, for the provision of X-ray free-electron laser beamtime at Scientific Instrument HED (High Energy Density Science) and would like to thank the staff for their assistance. Characterization of the initial sample was performed at the Stanford Nano Shared Facilities (SNSF), supported by the National Science Foundation under award ECCS-2026822. Part of this work was performed under the auspices of the U.S. Department of Energy by Lawrence Livermore National Laboratory under Contract DE-AC52-07NA27344. S.K. and H.K. acknowledge the support of the National Research Foundation of Korea grant NRF-2021R1A3B1077076.

References

1. W. Beere, Stresses and deformation at grain boundaries. *Philos. Trans. R. Soc. Lond. A* **288**, 177–196 (1978).
2. D. Moldovan, V. Yamakov, D. Wolf, and S. R. Phillpot, Scaling behavior of grain-rotation-induced grain growth. *Phys. Rev. Lett.* **89**, 206101 (2002).
3. R. Kobayashi, I. A. Warren, and W. C. Carter, A continuum model of grain boundaries. *Phys. D* **140**, 141–150 (2000).
4. M. Upmanyu, D. J. Srolovitz, A. E. Lobkovsky, J. A. Warren, and W. C. Carter, Simultaneous grain boundary migration and grain rotation. *Acta Mater.* **54**, 1707–1719 (2006).
5. X. Zhou, *et al.* Reversal in the Size Dependence of Grain Rotation. *Phys. Rev. Lett.* **118**, 096101 (2017).
6. N. Hansen, The effect of grain size and strain on the tensile flow stress of aluminium at room temperature. *Acta Metall.* **25**, 863 (1977).
7. A. Azizi, *et al.* Dislocation motion and grain boundary migration in two-dimensional tungsten disulphide. *Nat. Commun.* **5**, 4867 (2014).
8. K. E. Harris, V. V. Singh, and A. H. King, Grain rotation in thin films of gold. *Acta Mater.* **46**, 2623–2633 (1998).
9. S. I. Kim, *et al.* Dense dislocation arrays embedded in grain boundaries for high-performance bulk thermoelectrics. *Science* **348**, 109–114 (2014).
10. M. Murayama, J. M. Howe, H. Hidaka, S. Takaki, Atomic-level observation of disclination dipoles in mechanically milled, nanocrystalline Fe. *Science* **295**, 2433–2435 (2002).

11. R. L. Penn and J. F. Banfield, Imperfect oriented attachment: Dislocation generation in defect-free nanocrystals. *Science* **281**, 969–971 (1998).
12. Z. Shan, *et al.* Grain boundary-mediated plasticity in nanocrystalline nickel. *Science* **305**, 654–657 (2004).
13. B. Bay, N. Hansen, and D. Kuhlmann-Wilsdorf, Microstructural evolution in rolled aluminium. *Mater. Sci. Eng. A* **158**, 139-146 (1992).
14. F. M. Alcorn, *et al.* Time-resolved transmission electron microscopy for nanoscale chemical dynamics. *Nat. Rev. Chem.* **7**, 256-272 (2023).
15. L. Margulies, G. Winther, and H. F. Poulsen, In situ measurement of grain rotation during deformation of polycrystals. *Science* **291**, 2392–2394 (2001).
16. B. Jakobsen, *et al.* Formation and subdivision of deformation structures during plastic deformation. *Science* **312**, 889–892 (2007).
17. H. F. Poulsen, L. Margulies, S. Schmidt, and G. Winter, Lattice rotations of individual bulk grains Part I: 3D X-ray characterization. *Acta Mater.* **51**, 3821–3830 (2003).
18. C. E. Wehrenberg, *et al.* In situ X-ray diffraction measurement of shock-wave-driven twinning and lattice dynamics. *Nature* **550**, 496–499 (2017).
19. H. Yumoto, *et al.* High-fluence and high-gain multilayer focusing optics to enhance spatial resolution in femtosecond X-ray laser imaging. *Nat. Commun.* **13**, 5300 (2022).
20. S. Matsuyama, *et al.* Nanofocusing of X-ray free-electron laser using wavefront-corrected multilayer focusing mirrors. *Sci. Rep.* **8**, 17440 (2018).
21. K. Lu, Stabilizing nanostructures in metals using grain and twin boundary architectures. *Nat. Rev. Mater.* **1.5** 1-13 (2016).
22. J. M. Dake, *et al.* Direct observation of grain rotations during coarsening of a semisolid Al–Cu alloy. *Proc. Natl. Acad. Sci. USA* **113**, E5998–6006 (2016).
23. A. J. Haslam, *et al.* Combined atomistic and mesoscale simulation of grain growth in nanocrystalline thin films. *Comput. Mater. Sci.* **23**, 15–32 (2002).
24. E. R. Leite, *et al.* Crystal growth in colloidal tin oxide nanocrystals induced by coalescence at room temperature. *Appl. Phys. Lett.* **83**, 1566-1568 (1977).
25. K. Ichiyangi, *et al.* Microstructural deformation process of shock-compressed polycrystalline aluminum. *Sci. Rep.* **9**, 7604 (2019).
26. Q. Liu, Z. Xiong, X. Liu, L. Fang, C. Lv, J. Yang, Y. Liu, Y. Zhang, W. Zhu, J. Li, Y. Yu, and Z. Gao, Grain size dependence of grain rotation under high pressure and high temperature. *J. Appl. Phys.* **134**, 185903 (2023).
27. Z. Huang, Z. et al. Grain rotation and lattice deformation during photoinduced chemical

- reactions revealed by in situ X-ray nanodiffraction. *Nat. Mater.* **14**, 691–695 (2015).
28. I. Zizak, et al. Ion-beam-induced collective rotation of nanocrystals. *Phys. Rev. Lett.* **101**, 065503 (2008).
 29. J. Zhou, M. I. Islam, S. Guo, Y. Zhang, and F. Lu, Radiation-Induced Grain Growth of Nanocrystalline Al_xCoCrFeNi High-Entropy Alloys. *J. Phys. Chem. C*, **125**, 3509–3516 (2021).
 30. G. S. Was, *Fundamentals of Radiation Materials Science: Metals and Alloys* (Springer, 2007).
 31. U. Zastra, et al. The High Energy Density Scientific Instrument at the European XFEL. *J. Synchrotron Rad.* **28**, 1393–1416 (2021).
 32. T. Tschentscher, C. Bressler, J. Grünert, A. Madsen, A. Mancuso, M. Meyer, A. Scherz, H. Sinn, and U. Zastra, Photon Beam Transport and Scientific Instruments at the European XFEL. *Appl. Sci.* **7**, 592 (2017).
 33. K. Momma and F. Izumi, VESTA 3 for three-dimensional visualization of crystal, volumetric and morphology data. *J. Appl. Cryst.* **44**, 1272–1276 (2011).
 34. L. E. Dresselhaus-Marais, et al. Simultaneous bright- and dark-field X-ray microscopy at X-ray free electron lasers. *Sci. Rep.* **13**, 17573 (2023).
 35. A. Snigirev, V. Kohn, I. Snigireva, and B. Lengeler, A compound refractive lens for focusing high-energy X-rays. *Nature* **384**, 49–51 (1996).
 36. Z. Yu, et al. Structural phase transitions in Bi₂Se₃ under high pressure. *Sci. Rep.* **5**, 15939 (2015).
 37. See Supplemental Material.
 38. Y. Liu, Y. Y. Li, S. Rajput, D. Gilks, L. Lari, P. L. Galindo, M. Weinert, V. K. Lazarov, and L. Li *Nat. Phys.* **10**, 294-299 (2014).
 39. H. Okamoto, The Bi-Se (bismuth-selenium) system. *J. Phase Equilib.* **15** 195-201 (1994).
 40. M. L. Cafaro, G. Bardi, and V. Oiancente, Vaporization study of solid bismuth selenide (Bi₂Se₃). *J. Chem. Eng. Jpn.* **29**, 78 (1984).
 41. X. Chen, et al. Thermal expansion coefficients of Bi₂Se₃ and Sb₂Te₃ crystals from 10 K to 270 K. *Appl. Phys. Lett.* **99**, 261912 (2011).
 42. D. Moldovan, D. Wolf, and S. R. Phillpot, Theory of diffusion-accommodated grain rotation in columnar polycrystalline microstructures. *Acta Mater.* **49**, 3521–3532 (2001).
 43. L. Wang, et al. Grain rotation mediated by grain boundary dislocations in nanocrystalline platinum. *Nat. Commun.* **5**, 4402 (2014).

**Supplemental Materials for
X-ray induced grain structure dynamics in Bi₂Se₃**

Kento Katagiri^{1,2,3*}, Bernard Koziolowski⁴, Eric Folsom⁴, Yifan Wang^{1,2,3}, Karen Appel⁵,
Philip K. Cook⁶, Jon Eggert⁴, Sebastian Göde⁵, Marylesa Howard⁷, Sungwon Kim⁸,
Mikako Matsuda⁵, Motoaki Nakatsutsumi⁵, Martin M. Nielsen⁹, Henning F. Poulsen⁹,
Frank Seiboth¹⁰, Hugh Simons⁹, Bihan Wang¹¹, Wenge Yang¹¹, Ulf Zastra⁵, Hyunjung Kim⁸,
and Leora E. Dresselhaus-Marais^{1,2,3,4*}

¹*Stanford University, Department of Materials Science and Engineering, California 94305, USA*

²*SLAC National Accelerator Laboratory, California 94025, USA*

³*Stanford University, PULSE Institute, Stanford, 94305, California, USA*

⁴*Lawrence Livermore National Laboratory, California 94550, USA*

⁵*European XFEL GmbH, Schenefeld 22869, Germany*

⁶*University of Natural Resources and Life Sciences (BOKU), Institute for Physics and Materials Science, 1190 Vienna, Austria*

⁷*Nevada National Security Site, Nevada 89030, USA*

⁸*Sogang University, Department of Physics, Seoul 04107, Korea*

⁹*Technical University of Denmark, Department of Physics, Kgs. Lyngby 2800, Denmark*

¹⁰*Center for X-ray and Nano Science CXNS, Deutsches Elektronen-Synchrotron DESY, Notkestr. 85, 22607 Hamburg, Germany*

¹¹*Center for High-Pressure Science and Technology Advanced Research, Shanghai 201203, China*

*Corresponding authors. Email: kentok@stanford.edu & leoradm@stanford.edu

I. Structure of the Bi_2Se_3 sample under X-ray irradiation

The observed structure of the Bi_2Se_3 sample under X-ray irradiation is $R\text{-}3m$ (Figure S1), which is the stable phase of Bi_2Se_3 at ambient conditions. Our *in-situ* XRD measurements did not show any signs of phase transformations or decomposition into Bi and Se. The XRD profiles collected at 9.5 s (Figure S1) suggest the peak from (205) is much stronger than other peaks, indicating the grain rotations are mostly along the c -axis (normal to the basal plane), making its texture fiber-like.

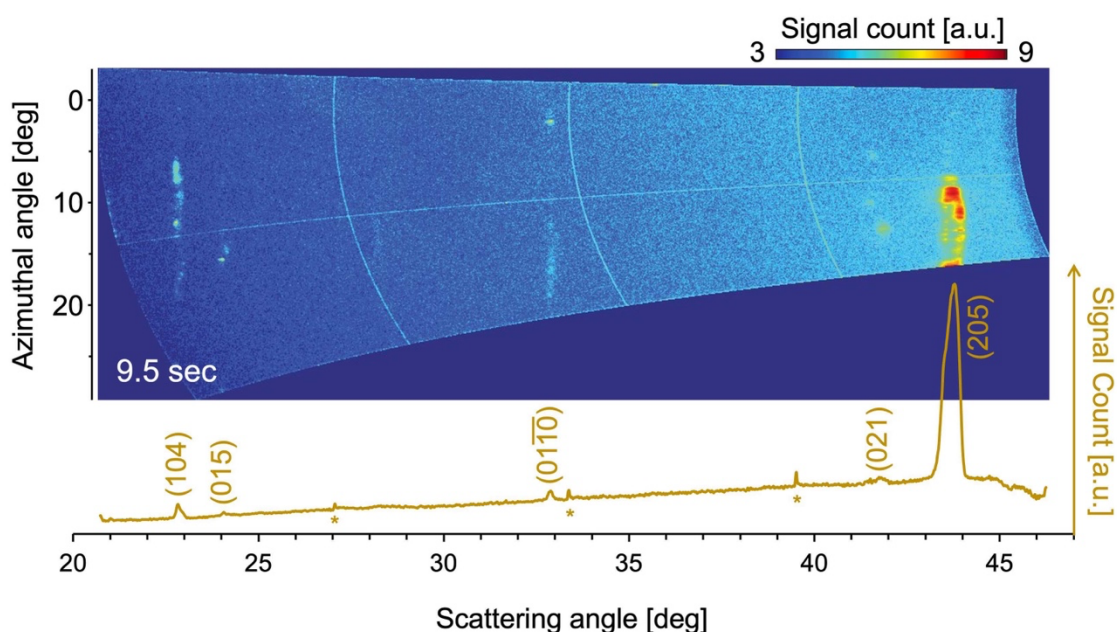


Figure S1. A polar-transformed version of the XRD image acquired at 9.5 s and the corresponding line profile. The XRD image has a color bar with an intensity that is logarithmically scaled for image clarity; the intensity of the corresponding line profile is scaled linearly. All the crystal planes denoted on the line profile are consistent with the $R\text{-}3m$ structure of the Bi_2Se_3 . The small and sharp peaks denoted with * are artifacts from detector junctions.

II. Temperature simulation based on the estimated XFEL pulse energy on the sample

In our experiments, the pulse energy of the XFEL was monitored by using an X-ray gas monitor (XGM) [44] located upstream of the sample. For the calibration runs, the average pulse energy XGM measured with an attenuator with 29% transmission was $\sim 120 \mu\text{J}$. For the run we presented in this work, we increased the transmission to 75%. By assuming the pulse energy before the attenuator to be the same between these runs, we have $120 \times 0.75 / 0.29 = 310 \mu\text{J/pulse}$ without attenuations. 97% of the beam was blocked by the 4-jaw slits located between the XGM and the sample, reducing the pulse energy to $8.7 \mu\text{J/pulse}$. Considering the attenuations from air and the diamond windows, we get $2.5 \mu\text{J/pulse}$ arriving on the front surface of the Bi_2Se_3 sample. The X-ray induced temperature rise in the $35 \mu\text{m}$ thick Bi_2Se_3 was then simulated by the COMSOL Multiphysics[®] [45] based on the estimated X-ray pulse energy onto the sample. The XFEL irradiation area was set as a $40 \mu\text{m}$ diameter circle in the simulation, which gives a beam size comparable to the measured beam size on the sample which is $32 \times 52 \mu\text{m}^2$. The simulated temperature profiles are shown in Figure 2.

III. Possible explanations for the observed grain boundary structures

Immediately after the (205) diffraction peak split into the three (or more) domains (Figure 4), two of the three diffraction peaks rotated towards different directions with a similar speed (See red and blue profiles at $\sim 8\text{-}9 \text{ s}$ in Figure 5C). This indicates that the temperature conditions that drive the grain rotations are similar for these grains, suggesting that these grains are located at the same depth from the X-ray irradiated side of the sample surfaces, as the predicted temperature distribution shows a strong dependence on the temperature on the distance from the X-ray irradiated surface. Therefore, we hypothesize that the grain rotation we observed is likely a “tilted” grain rotation rather than a “twisted” grain rotation (Figure S2) [46]. The insets in Figure 4b also illustrate the tilted type of grain rotations. The grain boundary formation between layers should be energetically more favorable than forming along the axis perpendicular to the layers. However, the grain boundaries perpendicular to the layers must be formed anyway because the initial crystal is larger than the XFEL beam size, meaning the rotation of the crystal would not occur without the grain boundary formations along the axis perpendicular to the layers. Therefore, we hypothesize that the energy barrier of grain boundary formation along the axis perpendicular to the layers would not hinder the occurrence of tilted grain rotations.

To have a better understanding of the structural evolution of the Bi_2Se_3 under the X-ray irradiation, we used a fast Fourier transform (FFT) filter for the image taken at 9.7 s (Figure S3).

The filtered image shows some long and curved lines. While these features may represent the structures of the damaged Bi_2Se_3 layers, the effect of shot-to-shot changes in the spatial beam profile of the XFEL cannot be separated.

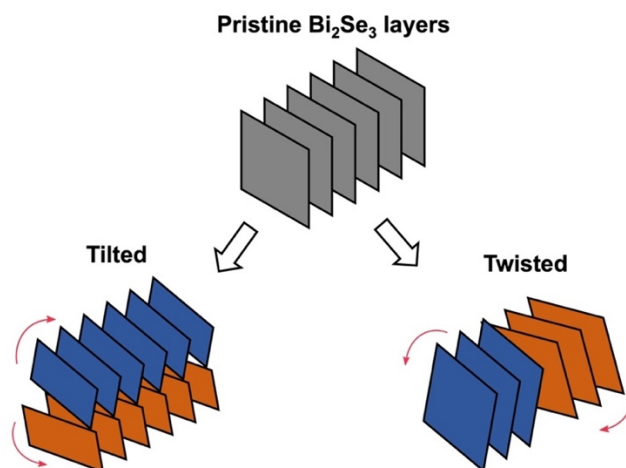


Figure S2. Two possible explanations for the observed grain boundary formation and grain rotations. Each plane shows a layer of Bi_2Se_3 . Rotating planes are colored blue and orange for better visibility. Rotation directions are indicated by the red arrows.

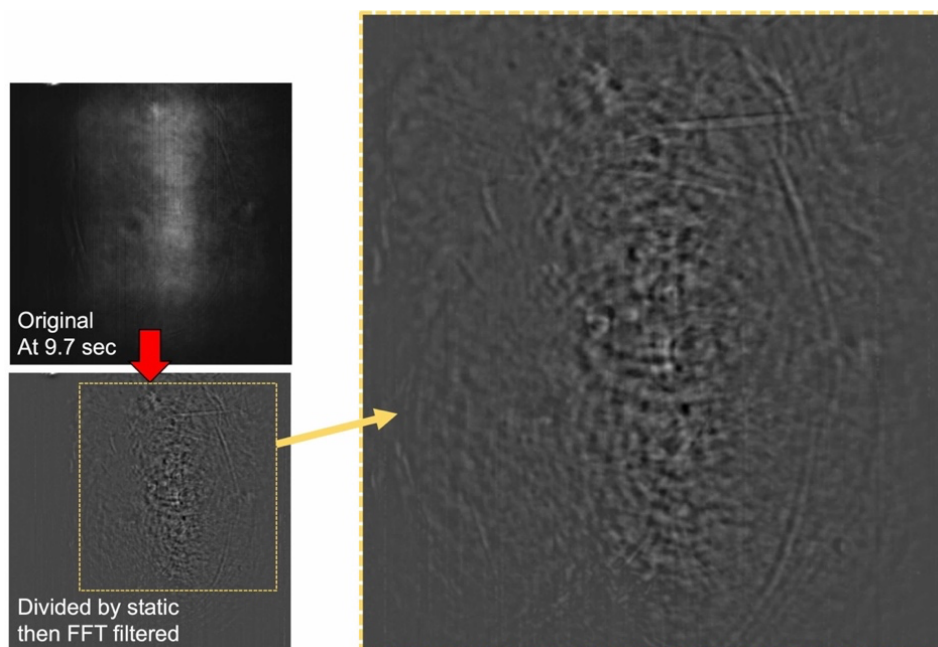


Figure S3. A fast Fourier transform (FFT) filtering of the TXM image at 9.7 s. Top-left image is the TXM image before FFT-filtering and is identical to the 9.7 s image shown in Figure 2. Bottom-

left image shows the FFT filtered image. The yellow dashed rectangle corresponds to the region where the enlarged image on the right shows.

References:

44. T. Maltezopoulos, *et al.*, Operation of X-ray gas monitors at the European XFEL. *J. Synchrotron Radiat.* **26.4**, 1045-1051 (2019).
45. Multiphysics C. Introduction to COMSOL multiphysics extregistered. COMSOL Multiphysics, Burlington, MA.
46. D. A. Porter and K. E. Easterling. Phase transformations in metals and alloys (revised reprint). CRC press, (2009).